Methodology to Develop Nonlinear State-Space Models for Active Control of Transonic Aeroelastic Phenomenon

Vasudevan, S.; Wang, Xuerui; De Breuker, R.

DOI
10.2514/6.2025-0623

Publication date
2025

Document Version
Final published version

Published in
Proceedings of the AIAA SCITECH 2025 Forum

AIAA SciTech Forum
6-10 January 2025, Orlando, FL
AIAA SCITECH 2025 Forum

10.2514/6.2025-0623

Methodology to Develop Nonlinear State-Space Models for Active Control of Transonic Aeroelastic Phenomena

Srikanth Vasudevan *, Xuerui Wang † and Roeland De Breuker‡
Delft University of Technology, Delft, The Netherlands

This paper aims to develop a reduced-order modelling methodology for nonlinear, unsteady, aerodynamic loads for active control transonic aeroelastic instabilities. To this end, a NACA0012 airfoil equipped with a flap is chosen as the test configuration. The aim here is to understand the interaction between the transonic shock dynamics and flap actuation at various amplitudes and frequencies. The high-fidelity simulations are carried out for two angles of attack, i.e. $\alpha = 0.0°, 4.0°$. It is found that transonic buffet characteristics significantly change with airfoil geometry. Additionally, the flap is seen to be ineffective in the separated flow regions, thereby making the C_l-β slopes highly nonlinear. However, increasing the frequencies of flap oscillations, increases flap effectiveness, increases control over buffet motion and moves towards linear lift responses. Furthermore, we also evaluate the performance of several Bayesian Filters that are crucial in the state-estimation process of the active control of nonlinear systems. It is observed that nonlinear filters such as Unscented Karman Filter perform better than the traditional linear Kalman Filter as system response to flap actuation becomes nonlinear in the presence of separated boundary layer.

I. Nomenclature

A	=	amplitude of oscillation
c	=	chord
F, G	=	functions for spatial nonlinear transformation
H	=	time-dependent nonlinear function describing latent-space dynamics
h	=	heave (m)
α	=	angle-of-attack / pitch (degrees)
β	=	flap angle (degrees)
M_{ae}, C_{ae}, K_{ae}	=	aeroelastic mass, damping and stiffness matrices
$F_a(t)$	=	unsteady aerodynamic force vector
$x, u, z, w, v, \chi, w_i^{(m)}, w_i^{(c)}$	=	State-Estimation model parameters
A, B, H, P, S, K	=	State-Estimation model matrices
KF, EKF, UKF,PF	=	Linear and Nonlinear Bayesian Filters
CFD, FEM	=	Computational Fluid Dynamics, Finite-Element Methods
AIC	=	Aerodynamic Influence Coefficients
GVT	=	Ground Vibration Tests
uRANS	=	Unsteady Reynolds Averaged Navier Stokes
LES	=	Large Eddy Simulations
DNS	=	Direct Numerical Simulations

*Ph.D. Candidate, Aerospace Structures and Materials, Faculty of Aerospace Engineering, Delft University of Technology, S.Vasudevan@tudelft.nl, Student member AIAA.

†Assistant Professor, Aerospace Structures and Materials, Faculty of Aerospace Engineering, Delft University of Technology, X.Wang-6@tudelft.nl, Senior member AIAA.

‡Associate Professor, Aerospace Structures and Materials, Faculty of Aerospace Engineering, Delft University of Technology, R.deBreuker@tudelft.nl, Associate Fellow AIAA.

II. Introduction

Active control of aeroelastic systems in the transonic regime presents itself as one of the most challenging topics with rich and complex physics that is yet to be fully understood. The aerodynamic flow field is inherently unsteady and nonlinear in this regime due to the presence of shock waves that exhibit dynamic motion. In addition, the structure could exhibit linear or nonlinear responses based on its stiffness and aspect ratio. This leads to a premature onset of instability in such coupled systems [1]. Thus, active control is imperative. Today, aircraft fly in the transonic dip without control. Owing to the differences in the dimensionality of each of these subsystems, design of efficient active control systems for such scenarios is not a trivial task.

In transonic flows over airfoils, the presence of partial supersonic bubbles makes the flow field neutrally stable, thus susceptible to instabilities such as the self-sustained limit cycle oscillations of the shock due to minor changes in the flow conditions [2]. This is termed as transonic buffeting [3–6]. As numerical models introduce marginal errors that could lead to drastically different long-term responses of such nonlinear systems, wind tunnel experiments should form the ground truth. However, limited wind tunnel data exists in literature due to challenging high operational costs of transonic wind tunnels.

In aeroservoelasticity (ASE), numerical models of the aircraft are developed via superposition of eigenmodes, as seen with the FLEXOP [7] and NASA X-56 [8] demonstrators. Dimensionality reduction is then performed on these large order systems [9–11], leading to low-order temporal state-space models. For active control, state-space representations are preferred due to their ability to incorporate nonlinearities, real-time adjustments to system responses, and superior disturbance rejection. However, since the classical aeroelastic problem is based on potential flow theory [12], the aforementioned nonlinear flow physics is missing.

Due to these limitations, we often rely on numerical simulations of the partial differential equations to obtain the spatio-temporal flow field. In particular, for unsteady transonic flows over airfoils, most commonly used CFD methods are unsteady Reynolds Averaged Navier-Stokes (uRANS), Detached-Eddy Simulations (DES) and Large Eddy Simulations (LES). In an abstract sense, these methods are analogous to low-pass filters of the wind tunnel tests with increasing cut-off frequencies. Although, numerical techniques such as shock capturing [13] and shock-fitting methods [14] based on Euler equations do exist, they fail to explain the origins of these instabilities from a theoretical perspective. The existence of a boundary layer is necessary to capture the interactions at the shock-foot that leads to the buffet. Additionally, one must also evaluate what fidelity of the aforementioned CFD methods is sufficient to capture the phenomenon of interest accurately. Reduced-Order Modelling (ROM) therefore requires a trade-off between accuracy and computational cost.

One approach is to use existing high-fidelity data to lower the computational overhead while generating the ROM. In aeroelasticity, CFD-based correction of the Aerodynamic Influence Coefficients (AIC) of potential flow codes and Ground Vibration Test (GVT) based Finite-Element (FE) model correction [7] and other CFD-based ROMs [15–18] are common instances of these data-driven techniques. In the recent past, with the rise in popularity of machine-learning algorithms [19–21], purely data-driven approaches are being developed, whose major limitation comes from the requirement of extensive amounts of data. However, Bayesian approaches are increasing being utilised for time-series forecasting [22, 23] and will be crucial in paving new avenues of research. It is interesting to observe that the fundamental building blocks of many machine learning algorithms are statistical tools that can be derived from first principles. Active control can also be viewed as a time-series forecasting task. Bayesian approaches play a crucial role in these procedures to infer the model dynamics, termed as state estimation.

It is, therefore, evident that in order to achieve fast and accurate predictions, combining both physics-based and data-based simulations is key. This ensures analytical and numerical tracability. Thus, the ideal optimisation strategy is to maximise the physics-based part by developing representative low-order analytical models [24] which can then be cast into a nonlinear state-space form. Furthermore, a data-driven strategy to include additional parametric effects into the low-order model will improve accuracy. This is illustrated in the Figure 1 below.

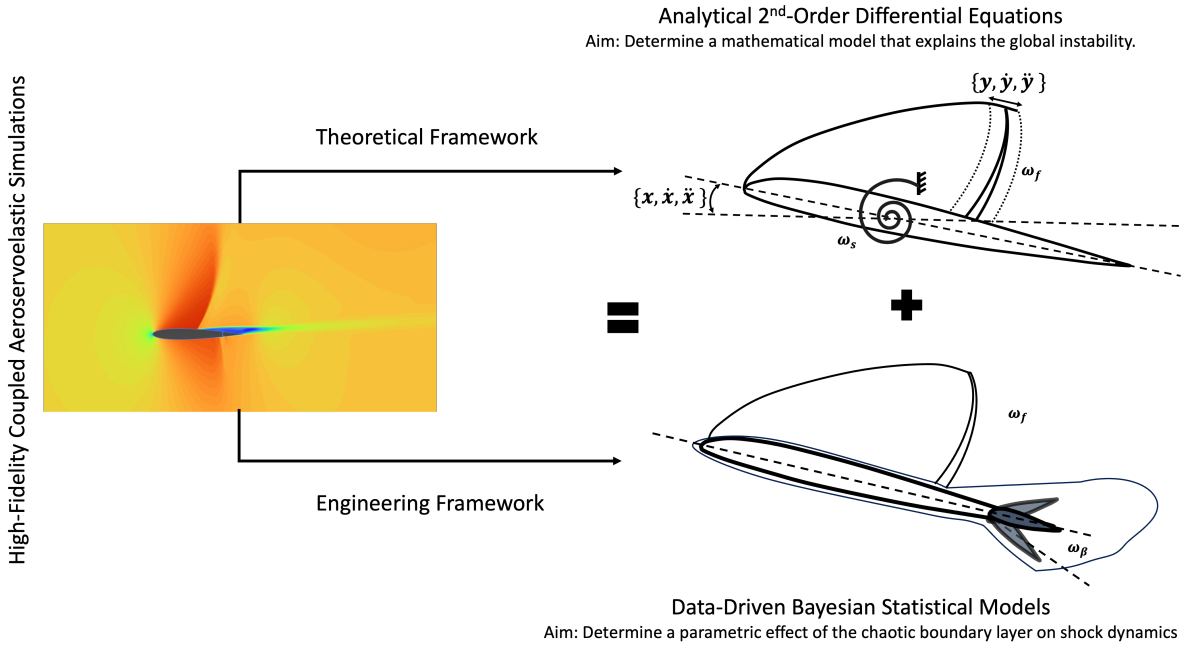

Fig. 1 Methodology to solve the transonic aeroelastic problem.

In this work, we study the nonlinear effects of the flap actuation on the shock dynamics using high fidelity simulations and evaluate its effectiveness. Futhermore, we evaluate the ability of nonlinear control algorithms to estimate the hidden states of the nonlinear system from data. This study contributes in part towards the generation of nonlinear state-space models for active-control of transonic aeroelastic systems.

This paper is structured as follows: Section III briefly illustrates the methodologies that will be adopted for the numerical models summarised above. Section IV presents and discusses the obtained results and their implications. Finally, section V presents the major conclusions.

III. Details of the Transonic Simulations and State Estimation Methods

This section presents the numerical settings that were used for the high fidelity transonic simulations in III.A. The mathematical background for the control algorithms are presented in III.B in detail.

A. High Fidelity Problem Description

Without loss of generality, a NACA0012 airfoil has been chosen as the airfoil geometry for the current study. The aim is to study the possibility of controlling the shock motion via active control methods. To this end, the chosen airfoil is equipped with a flap of length $0.2c$ at the trailing edge with an airfoil-flap gap of x_g = 5 mm as shown in Figure 2a. $\alpha, \beta, x(t)$ are the angle of attack, flap deflection angle and shock location respectively. β has a positive deflection downwards. An unstructured mesh grid, shown in Figure 2b is used for this study due to the complexities involved with structured dynamic meshes [25], especially around the small gap region between the airfoil and the flap. In addition, a realistic CFD simulation over complex geometries such as 3D wing structures are often carried out using unstructured meshes.

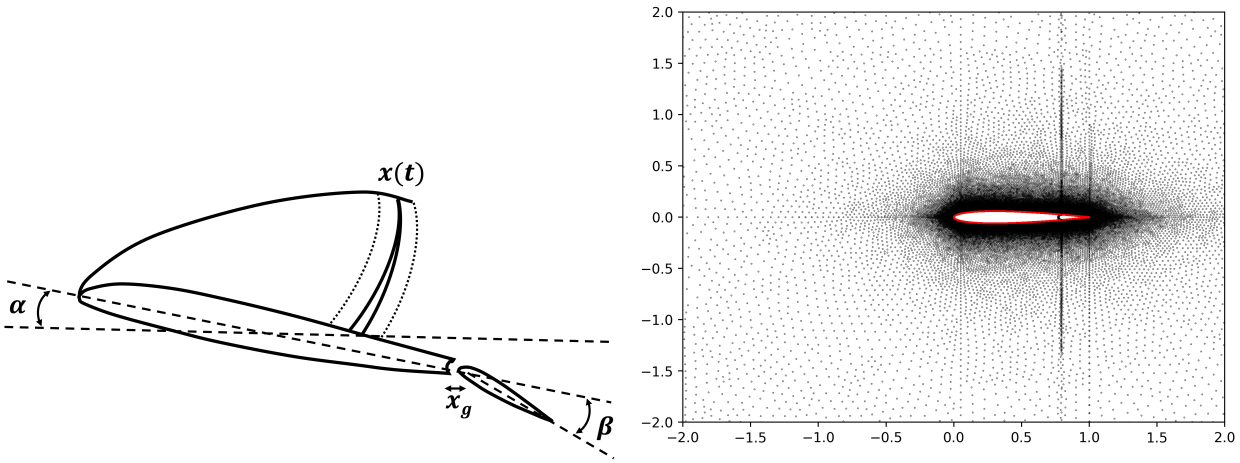

(a) Airfoil-flap geometry illustrating the gap x_g = 5 mm. **(b) Unstructured mesh with refinement around the gap.**

Fig. 2 Geometry and mesh description of the uRANS simulation at $M = 0.82$.

Ansys Fluent 2024R2 was used for the flow simulations in this work. Table 1 briefly summarises the settings used for the dynamic unsteady simulations over the airfoil-flap geometry. The settings are consistent with our previous related work [24]

Table 1 CFD Simulation Settings (adapted from [24]).

Property	Definition
Bounding Box	15X × 10X (X is the airfoil chord)
Mesh Domain	Unstructured mesh with $\approx 1.0 \times 10^6$ nodes
Airfoil geometry	NACA0012, $c = 1.0$ m, $l_f = 0.2$ c, $\alpha = 0.0°, 4.0°$
Flow settings	Spalart Allaramas uRANS model, $M = 0.82$

The simulations in this work can be classified into two major test cases, i.e. (a) $\alpha = 0.0°$, (b) $\alpha = 4.0°$. Each test case further consists of 2 amplitudes of flap oscillations, i.e (a) $\Delta\beta = \pm 5.0°$, (b) $\Delta\beta = \pm 10.0°$. Thus, a total of four temporal unsteady simulations were carried out for this study. The prescribed unsteady flap oscillation is purely sinusoidal and has the form $\beta_f(t) = \beta_0 \sin(\omega T)$. The total simulation time was $t = 6.5$s with $\Delta t = 0.001$s Additionally, after every 2 seconds, the flap oscillation frequency was increased according to the list $f(Hz) = \{0, 1, 10, 20\}$ for all amplitudes.

B. State Estimation using Nonlinear Bayesian Filters

Bayesian Filters are control frameworks for estimating the states of a dynamical system. They are built on a probabilistic approach to iteratively update the beliefs about the system behaviour from the most recent measurement data. This section presents the mathematical formulation of the Bayesian Filter. For the sake of brevity, only the algorithmic steps are provided here. For the detailed derivations, interested readers are referred to [26, 27]. For implementation, python library FilterPy [28] can be used. To begin with, we will look at the Kalman Filter.

Consider the state-space representation of the system is being modelled as :

$$\text{State Equation:} \quad \mathbf{x}_k = \mathbf{A}\mathbf{x}_{k-1} + \mathbf{B}\mathbf{u}_k + \mathbf{w}_k,$$

$$\text{Measurement Equation:} \quad \mathbf{z}_k = \mathbf{H}\mathbf{x}_k + \mathbf{v}_k,$$

where:

- $\mathbf{x}_k$: State vector at time k,
- $\mathbf{u}_k$: Control input,
- $\mathbf{z}_k$: Measurement vector,
- $\mathbf{A}$: State transition matrix,
- $\mathbf{B}$: Control matrix,
- $\mathbf{H}$: Observation matrix,
- $\mathbf{w}_k$: Process noise ($\mathbf{w}_k \sim \mathcal{N}(\mathbf{0}, \mathbf{Q})$),
- $\mathbf{v}_k$: Measurement noise ($\mathbf{v}_k \sim \mathcal{N}(\mathbf{0}, \mathbf{R})$).

1. The predictor-corrector algorithm

The filter predicts the next state and the error covariance:

$$\text{Predicted State:} \quad \hat{\mathbf{x}}_{k|k-1} = \mathbf{A}\hat{\mathbf{x}}_{k-1|k-1} + \mathbf{B}\mathbf{u}_k,$$

$$\text{Predicted Covariance:} \quad \mathbf{P}_{k|k-1} = \mathbf{A}\mathbf{P}_{k-1|k-1}\mathbf{A}^\top + \mathbf{Q}.$$

Where, $\hat{\boldsymbol{x}}_{\boldsymbol{k|k-1}}$ and $\hat{\boldsymbol{P}}_{\boldsymbol{k|k-1}}$ are the conditional predictions of the state and the covariance given previous measurements.

In the next iteration, when a new measurement is received, the filter performs a correction often referred to as the Update step:

1) Compute the Kalman Gain:
$$\mathbf{K}_k = \mathbf{P}_{k|k-1}\mathbf{H}^\top \left(\mathbf{H}\mathbf{P}_{k|k-1}\mathbf{H}^\top + \mathbf{R}\right)^{-1}.$$
2) Update the State Estimate:
$$\hat{\mathbf{x}}_{k|k} = \hat{\mathbf{x}}_{k|k-1} + \mathbf{K}_k \left(\mathbf{z}_k - \mathbf{H}\hat{\mathbf{x}}_{k|k-1}\right).$$
3) Update the Covariance:
$$\mathbf{P}_{k|k} = \left(\mathbf{I} - \mathbf{K}_k\mathbf{H}\right)\mathbf{P}_{k|k-1}.$$

Similarly, $\hat{\boldsymbol{x}}_{\boldsymbol{k|k}}$ and $\hat{\boldsymbol{P}}_{\boldsymbol{k|k}}$ are the conditional updates of the state and the covariance given predicted values. $\boldsymbol{K_k}$ is the Kalman Gain, which is a measure of how much the predicted values must be adjusted.

2. Unscented Kalman Filter

The Unscented Kalman Filter (UKF) extends the aforementioned algorithm to handle nonlinearities by approximating the state distribution a sampling procedure that is termed as unscented transform. Due to this reason, UKF is more efficient than the Extended Kalman Filter (EKF) which computes the gradient at each prediction step.

The algorithm begins with the Sigma Point ($\chi_{i,k-1}$) selection to approximate the state distribution.

$$\chi_{i,k-1} = \hat{\mathbf{x}}_{k-1|k-1} + \sqrt{(n+\lambda)\mathbf{P}_{k-1|k-1}}_i,$$

where n is the state dimension and λ is the scaling parameter:

Next, is the prediction step :

1) Propagate each sigma point:
$$\chi_{i,k|k-1} = f(\chi_{i,k-1}, \mathbf{u}_k).$$
2) Compute the predicted mean and covariance:
$$\hat{\mathbf{x}}_{k|k-1} = \sum_i w_i^{(m)} \chi_{i,k|k-1},$$
$$\mathbf{P}_{k|k-1} = \sum_i w_i^{(c)} \left(\chi_{i,k|k-1} - \hat{\mathbf{x}}_{k|k-1}\right)\left(\chi_{i,k|k-1} - \hat{\mathbf{x}}_{k|k-1}\right)^\top + \mathbf{Q}.$$

$w_i^{(m)}$ and $w_i^{(c)}$ are the weights for computing the mean and covariance.
Finally, the update step is given as:

1) Propagate sigma points (ζ) through the measurement function:

$$\zeta_{i,k} = h(\chi_{i,k|k-1}).$$

2) Compute the predicted measurement mean ($\hat{\mathbf{z}}$) and covariance ($\mathbf{S}$):

$$\hat{\mathbf{z}}_k = \sum_i w_i^{(m)} \zeta_{i,k},$$

$$\mathbf{S}_k = \sum_i w_i^{(c)} \left(\zeta_{i,k} - \hat{\mathbf{z}}_k\right) \left(\zeta_{i,k} - \hat{\mathbf{z}}_k\right)^\top + \mathbf{R}.$$

3) Compute the cross-covariance ($\mathbf{P}_{xz}$):

$$\mathbf{P}_{xz} = \sum_i w_i^{(c)} \left(\chi_{i,k|k-1} - \hat{\mathbf{x}}_{k|k-1}\right) \left(\zeta_{i,k} - \hat{\mathbf{z}}_k\right)^\top.$$

4) Update state ($\hat{\mathbf{x}}$) and covariance ($\mathbf{P}$):

$$\mathbf{K}_k = \mathbf{P}_{xz}\mathbf{S}_k^{-1},$$
$$\hat{\mathbf{x}}_{k|k} = \hat{\mathbf{x}}_{k|k-1} + \mathbf{K}_k \left(\mathbf{z}_k - \hat{\mathbf{z}}_k\right),$$
$$\mathbf{P}_{k|k} = \mathbf{P}_{k|k-1} - \mathbf{K}_k\mathbf{S}_k\mathbf{K}_k^\top.$$

IV. Results and Discussions

Section IV.A presents the high-fidelity results for transonic simulations around NACA0012 for two angles of attack at $M = 0.82$, i.e $\alpha = 0.0°$ and $\alpha = 4.0°$. For each angle of attack, flap oscillations of varying amplitudes and frequencies are prescribed. The results presented in this section forms the ground truth for downstream processing of the effect of flap oscillations on the shock motion. Furthermore, Section IV.B evaluates the performance of the data-driven methodology proposed in Section III.B.

A. Effect of Sinusoidal Flap Oscillations on Shock Dynamics

The unsteady flow field obtained for the geometry presented in Section III.A illustrates the complex dynamics associated with transonic flows. In particular, this paper adapts the NACA0012 profile from the authors' previous work [24] to include a flap of length 0.2c. This introduces a small gap of 5mm between the airfoil and the flap. Interestingly, this inturn has resulted in a drop in the buffet frequency from previously obtained value of 25 Hz at $\alpha = 4.0°$ [24]. As expected, for $\alpha = 0.0°$, no shock buffet occurs as the design point $M = 0.82, \alpha = 0.0°$ lies within the aerodynamic buffet boundary and thus the shock is stable. The design point $M = 0.82, \alpha = 4.0°$ was chosen as this was found to be at buffet boundary for the NACA0012 airfoil [29].

Figure 3 presents snapshots of the representative pressure coefficient, C_p, of the unsteady flow field for the two test cases. The distinctive feature of the $\alpha = 0.0°$ test case is the presence of symmetric supersonic bubbles on either side of the airfoil, giving rise to interesting dynamics when there exists a relative motion of these shock locations.

In contrast, the $\alpha = 4.0°$ case shown on the right exhibits a consistent supersonic region only on the suction side. In particular, this test case of $M = 0.82, \alpha = 4.0°$ is chosen here as several studies have found this to be the crucial point where a transition to self-sustained oscillation of the flow occurs [29].

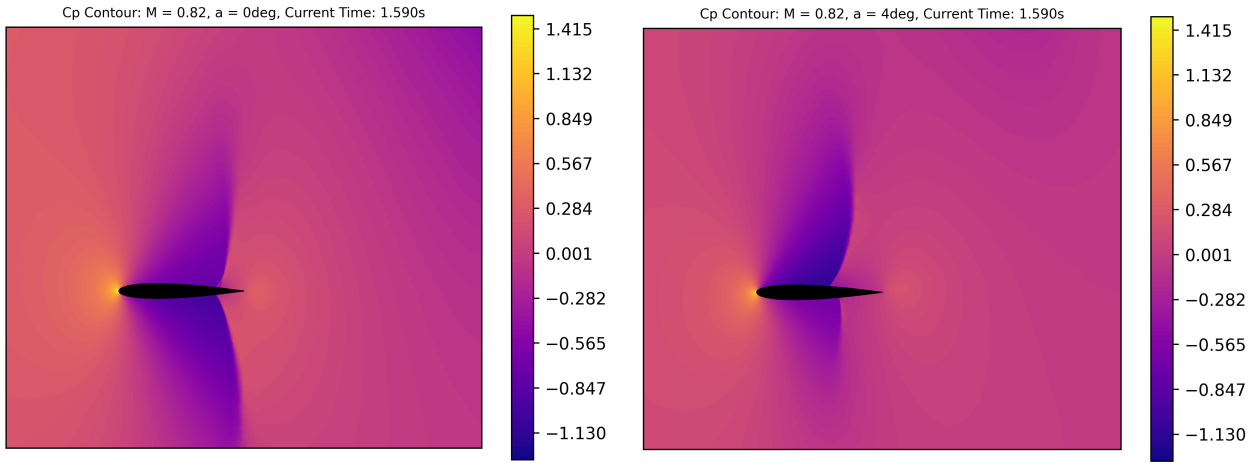

Fig. 3 Representative contour plots of the transonic pressure coefficient for the two test cases: (Left) α = 0.0° (Right) α = 4.0°.

Figure 4 presents the unsteady variation in the lift coefficient for the two test cases in response to prescribed sinusoidal flap oscillations of varying amplitudes and frequencies. By comparing lift variations from $t = 0$ s to $t = 2$ s (steady-state response with no flap deflection), we can observe the transition to the self-sustained oscillation, i.e. shock buffeting, as we move from $\alpha = 0°$ to $\alpha = 4°$. In addition, we also observe a mean negative c_l for $\alpha = 0.0°$. This is observed to be a result of unequal strengths of supersonic bubbles having a relative motion.

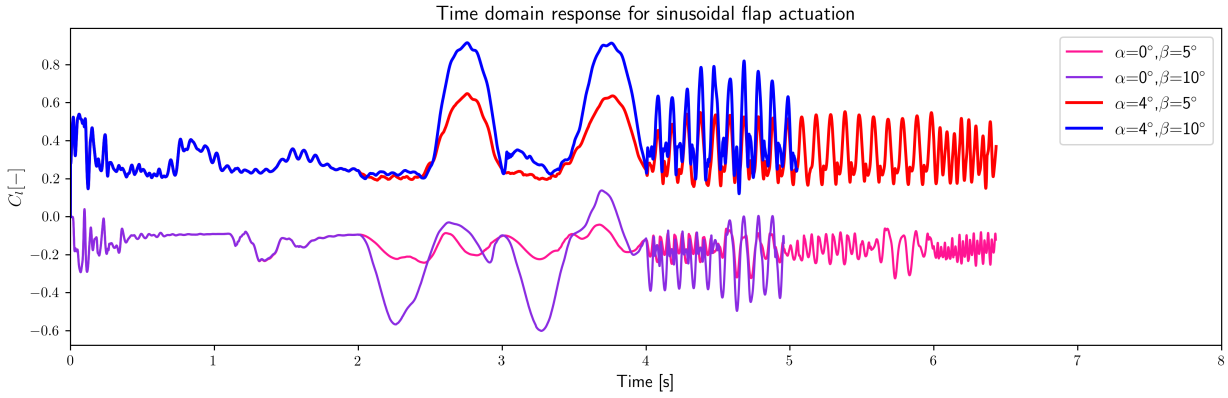

Fig. 4 Unsteady variation of the transonic lift coefficient for prescribed flap oscillation amplitudes and frequencies.

In figure 4, from $t = 2$ s to $t = 4$ s, the flap frequency is $f_\beta = 1$ Hz. For $\alpha = 0.0°$, the flap is observed to have effectiveness for both positive and negative deflection angles, although not equal. This is attributed to the relative strengths of the moving shocks on either side. For $\alpha = 4.0°$, the flap is observed to be effective only for a part of the cycle for both amplitudes. This is expected as the flap now operates partially within the separated boundary layer, whose height extends from the suction-side shock foot location to the trailing edge location in the vertical direction. Next, between $t = 4$ s and $t = 6$ s, the flap frequency is increased to $f_\beta = 10$ Hz. This frequency is chosen to understand the energy transfer mechanism between a prescribed oscillation close to the the natural buffet frequency $f_b = 12$ Hz. Particularly, for the $\alpha = 0.0°$ case, an interesting pattern is observed. This is because, the shock oscillates about two locations, one on the main airfoil and the other on the flap. This could be explained in terms of the gap that exists in the geometry, which acts as a natural barrier for the shock motion. Additionally, from $t = 6$ s, we also plot the response of

the transonic flow field to a flap oscillation frequency of $f_\beta = 20$ Hz. In this period, the variation in the lift coefficient is a direct function of the prescribed flap oscillations, indicating that the flap is in control of the shock dynamics.

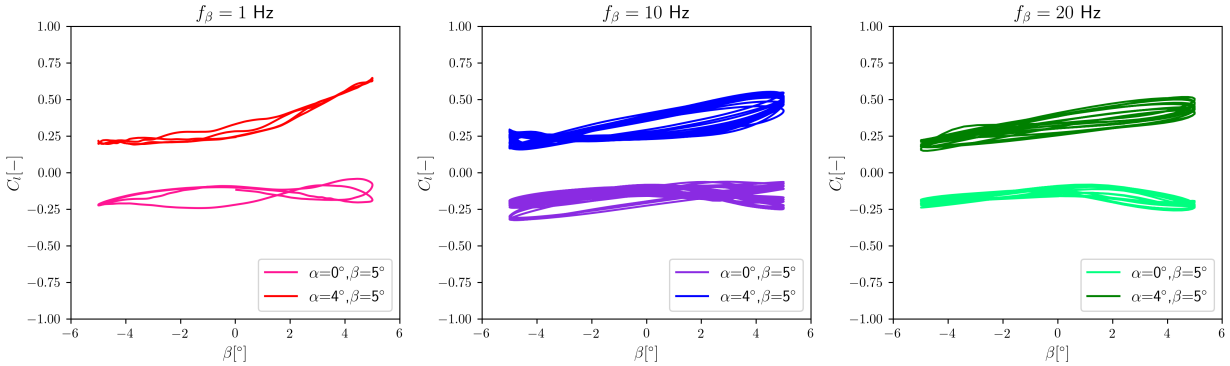

(a) $\beta = \pm 5°$: (left) $f_\beta = 1$ Hz, (middle) $f_\beta = 10$ Hz (right) $f_\beta = 20$ Hz.

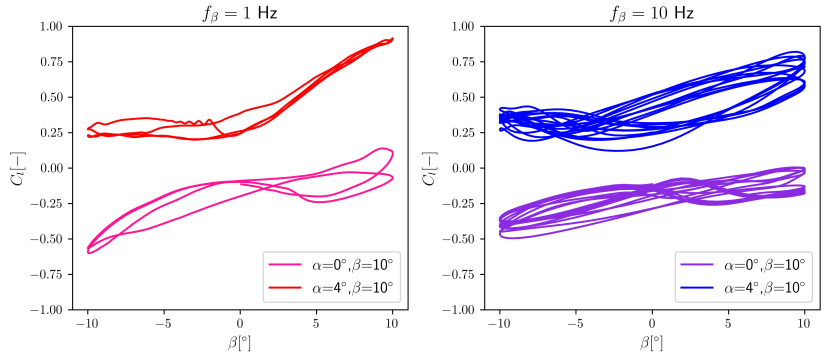

(b) $\beta = \pm 10°$: (left) $f_\beta = 1$ Hz, (right) $f_\beta = 10$ Hz.

Fig. 5 Effect of flap amplitude on coefficient of lift: (a) $\beta = \pm 5°$ (b) $\beta = \pm 10°$.

Figure 5 depicts the variation in the lift response as a function of flap angle β. The subplots in Figure 5a present the effect of flap frequency f_β for $\beta = \pm 5°$ amplitude. For $\alpha = 0.0°$, the lift response is independent of the flap oscillation frequency. However, for $\alpha = 4.0°$, increasing the flap frequency, increases the effectiveness of the flap. In particular, once the flap frequency exceeds a set threshold, the shock motion is fully controlled by the flap motion. This is a direct correlation with the amount of time the flap moves within the separated boundary layer. Similarly, Figure 5b presents the frequency effects for $\beta = \pm 10°$. Here, it is interesting to note that for $\alpha = 0.0°$, the C_l-β slope is no longer 0. The higher amplitude tends to exceed the boundary layer thickness, thereby making the flap effective. However, one can also observe the magnified effects of the boundary layer in $\alpha = 4.0°$ case. Once again, the flap is not effective in the separated region.

1. Angle of Attack

Increasing the angle of attack increases the lift response but also increases the separated boundary layer, thereby making the flap ineffective upto certain actuation angles. While for $\alpha = 0.0°$, the flap is symmetrically effective. Additionally for $\alpha = 0.0°$ between $t = 0$ s and $t = 4$ s with no flap actuation, a slight negative C_l is obtained. This is attributed to the relative shock position on either side.

2. Amplitude Effects

Increasing the amplitude of oscillations, increases the effectiveness of the flap, but also enhances the boundary layer effects at lower frequencies as the flap is immersed in the separated layer for a larger part of the cycle.

B. Performance of Bayesian Filters in Nonlinear State Estimation for Active Control

As seen in the previous section, the response of the aerodynamic system to the sinusoidal flap deflection is significantly nonlinear. In this section, we discuss the performance of Bayesian filters in the nonlinear state estimation process. In order to actively control a system, we need to measure a certain parameter, determine the relation between the measured parameter and the system state, and finally, develop closed-loop control laws that actively alter the dynamics of the states. For this, a crucial precusor is the state-estimation process, where the goal is to identify the hidden states, which are often functions of the measurement data. In particular, we compare the traditional Kalman Filter (KF) against the Unscented Kalman Filter (UKF). While both belong to the class of Bayesian Filters, the former assumes and formulates all probabilities to be Linear Gaussians. The latter is a nonlinear filter.

In order to simplify the problem, we present a test case as follows: we assume that there exists a direct correlation between the unsteady lift coefficient $C_l(t)$ and the shock location $x(t)$, which is often unknown and might be thought of as the hidden state. For this study, we consider the unsteady lift responses obtained in the previous section to be the measurement data as well as the hidden states. Thereby making the estimated states to be the same as the unsteady lift. In this manner, we can directly compare the convergence of the various filters towards the nonlinear lift while measuring the mean and variance of the dataset.

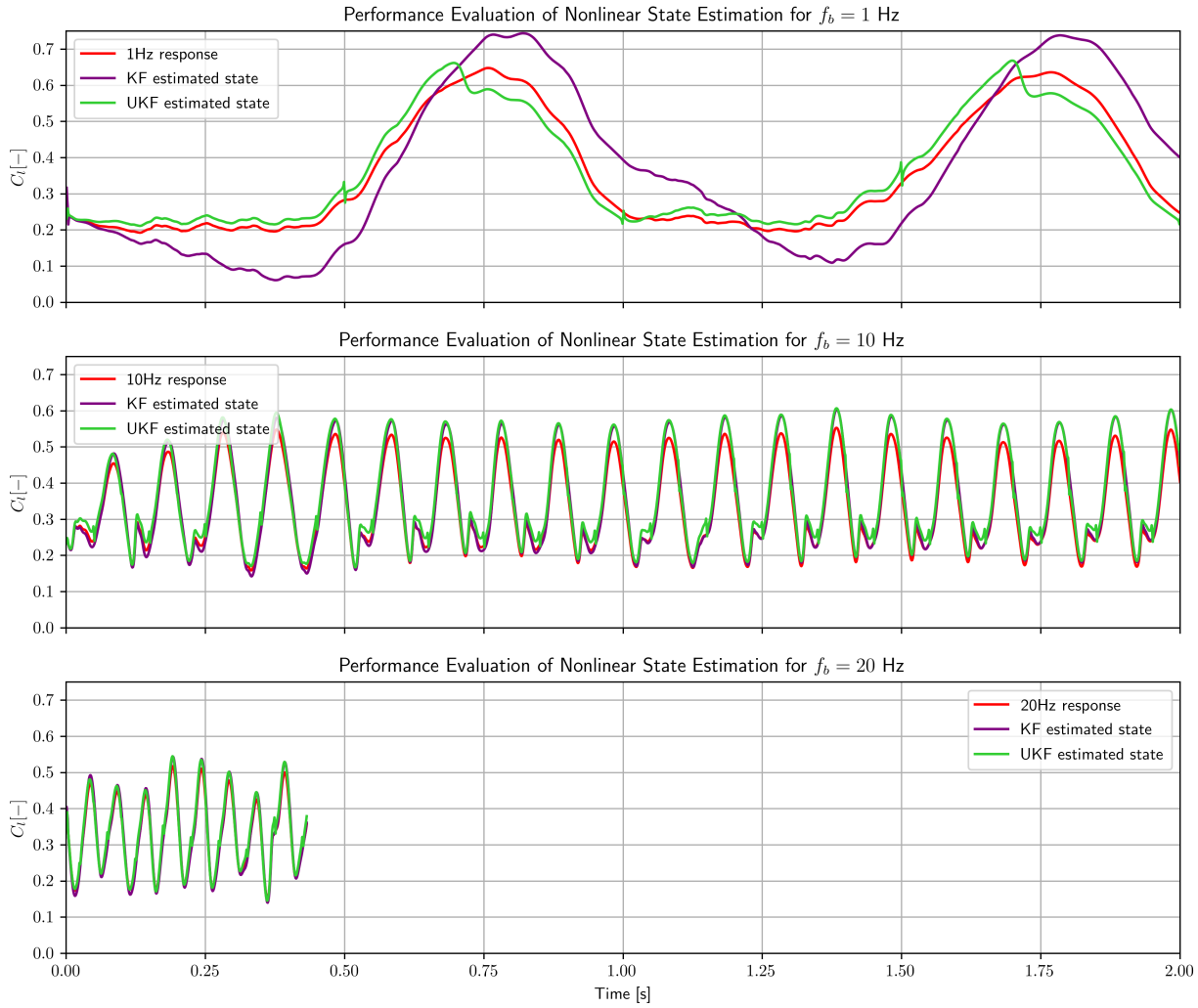

Fig. 6 Performance evaluation of nonlinear filters in state estimation.

Figure 6 shows the performance of the Kalman Filter (KF) and Unscented Kalman Filter (UKF) for various frequency ranges. The state equation is assumed to be similar to a second order system due to the presence of sinusoidal oscillations. Due to the assumption of equivalence of hidden and measurements states, the measurement equation is straightforward. The parameters of the system dynamics matrix are representative and are tuned to obtain accurate estimates. It is interesting to note that the state estimation capabilities of the Kalman filter improves as the frequency of flap oscillation increases. This confirms our previous observation that the system response becomes linear as the flap spends less time in the separated region. This is also expected from the Kalman filter as it is primarily a linear gaussian filter. For $f_\beta = 1$ Hz case on the top, the estimated state is incorrect due to presence of extreme nonlinearities. The flap is essentially ineffective for half the cycle.

Figure 6 also presents the improved predictions from the Unscented Kalman Filter (UKF) in green. The major improvement is seen in the most nonlinear low-frequency range. However, predictions for the high-frequency oscillations are comparable with those from Kalman filters. In the future, other non-linear filters will be further evaluated, such as the Particle Filter (PF).

V. Conclusions and Recommendations

In this work, we conduct a study on the effectivenes of flap actuation in controlling the shock motion. To this end, we obtain the unsteady lift responses to dynamic flap actuation in transonic conditions of $M = 0.82$ at angles $\alpha = 0.0^\circ$ and 4.0° over a NACA0012 airfoil via uRANS simulations using ANSYS Fluent.

The unsteady lift obtained from the high-fidelity simulations exhibit interesting dynamics with flap actuation direction, amplitudes and frequencies. The dynamic responses obtained here are different from our previous work due to the inclusion of the a flap with a gap of 5 mm from the main airfoil. From an aerodynamic standpoint, this change in geometry makes a significant change in the buffet frequency. From all the test cases analysed, the following effects can be observed:

1) Increasing the angle of attack, increases the lift response but also increases the separated boundary layer, thereby making the flap ineffective upto certain actuation angles. While for $\alpha = 0.0^\circ$, the flap is symmetrically effective.
2) Increasing the amplitude of oscillations, increases the effectiveness of the flap, but also amplifies the effect of the boundary layer at lower frequencies as the flap is immersed in the separated layer for a larger part of the cycle.

Furthermore, for non-linear filtering techniques, the following points are observed:

1) Bayesian filters are effective statistical tools for determining the nonlinear dynamics of complex systems.
2) A linear Kalman Filter, although ubiquitous, suffers from nonconvergence when nonlinearities are present.
3) The nonlinear Unscented Kalman Filter (UKF) out-performs the linear filter in all the cases.
4) For high frequency flap oscillations, both the filters have superior performance in terms of accurate identification of the hidden states as the system becomes linear. This is also an important conclusion for control law development for such systems.

VI. Future Work

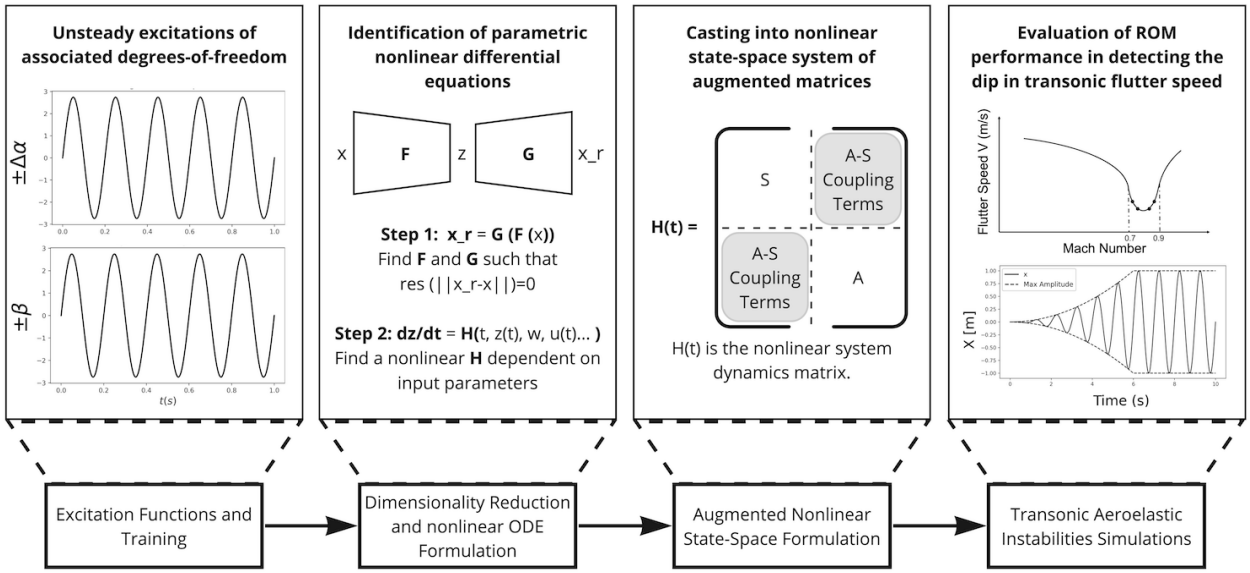

Fig. 7 Envisioned nonlinear reduced order modelling procedure.

Figure 7 illustrates the procedure that will be followed to develop the nonlinear aerodynamic reduced order model. It is known that the aeroelastic flutter is a type of a Hopf bifurcation. Thus, the input excitation signals that form the training dataset are oscillatory and include a wide range of frequencies. By obtaining a latent-space representation of the unsteady aerodynamic loads, one can determine the nonlinear evolution of the states of the system. Next, we obtain an augmented nonlinear state-space model that couples the fluid states to the structural states. Ideally, the obtained state-space matrices are time-dependent and hence the Jacobian (gradient) matrix is expected to be a function of time. Finally, we look at the open loop transonic flutter predictions of the reduced order model and compare them to the high-fidelity aero-structural simulations.

VII. Acknowledgements

The authors give special thanks to the Faculty of Aerospace Engineering of TU Delft for supporting this research, which is part of the Smart Flying-V project that addresses key technological challenges to enable unconventional aircraft configurations.

References

[1] Voß, R., Tichy, L., and Thormann, R., "A ROM based flutter prediction process and its validation with a new reference model," *Proceedings" IFASD 2011"*, 2011.

[2] Lee, B., "Self-sustained shock oscillations on airfoils at transonic speeds," *Progress in Aerospace Sciences*, Vol. 37, No. 2, 2001, pp. 147–196.

[3] Tijdeman, H., "Investigations of the transonic flow around oscillating airfoils," *NLR-TR 77090 U*, 1977.

[4] Feldhusen-Hoffmann, A., Statnikov, V., Klaas, M., and Schröder, W., "Investigation of shock–acoustic-wave interaction in transonic flow," *Experiments in Fluids*, Vol. 59, 2018, pp. 1–13.

[5] Korthäuer, T., Accorinti, A., Scharnowski, S., and Kähler, C. J., "Effect of Mach number and pitching eigenfrequency on transonic buffet onset," *AIAA Journal*, Vol. 61, No. 1, 2023, pp. 112–124.

[6] Raveh, D., and Dowell, E., "Aeroelastic Responses of Spring-suspended Airfoil Systems in Transonic Buffeting Flows," *53rd AIAA/ASME/ASCE/AHS/ASC Structures, Structural Dynamics and Materials Conference 20th AIAA/ASME/AHS Adaptive Structures Conference 14th AIAA*, 2012, p. 1630.

[7] Meddaikar, Y. M., Dillinger, J., Klimmek, T., Krueger, W., Wuestenhagen, M., Kier, T. M., Hermanutz, A., Hornung, M., Rozov, V., Breitsamter, C., et al., "Aircraft aeroservoelastic modelling of the FLEXOP unmanned flying demonstrator," *AIAA scitech 2019 forum*, 2019, p. 1815.

[8] Ouellette, J. A., "X-56A MUTT: Aeroservoelastic Modeling," Tech. rep., 2015.

[9] Lieu, T., Farhat, C., and Lesoinne, M., "POD-based aeroelastic analysis of a complete F-16 configuration: ROM adaptation and demonstration," *46th AIAA/ASME/ASCE/AHS/ASC structures, structural dynamics and materials conference*, 2005, p. 2295.

[10] Amsallem, D., Zahr, M. J., and Farhat, C., "Nonlinear model order reduction based on local reduced-order bases," *International Journal for Numerical Methods in Engineering*, Vol. 92, No. 10, 2012, pp. 891–916.

[11] Amsallem, D., Farhat, C., and Lieu, T., "Aeroelastic analysis of F-16 and F-18/A configurations using adapted CFD-based reduced-order models," *48th AIAA/ASME/ASCE/AHS/ASC structures, structural dynamics, and materials conference*, 2013, p. 2364.

[12] Theodorsen, T., "General theory of aerodynamic instability and the mechanism of flutter," Tech. rep., 1949.

[13] Toro, E. F., *Riemann solvers and numerical methods for fluid dynamics: a practical introduction*, Springer Science & Business Media, 2013.

[14] Salas, M. D., "Shock fitting method for complicated two-dimensional supersonic flows," *Aiaa Journal*, Vol. 14, No. 5, 1976, pp. 583–588.

[15] Lancelot, P., and De Breuker, R., "Unsteady Non-linear Control Surface Modelling for Aeroservoelastic Applications," *Journal of Aeroelasticity and Structural Dynamics*, Vol. 8, No. 1, 2021.

[16] Lieu, T., and Farhat, C., "Adaptation of aeroelastic reduced-order models and application to an F-16 configuration," *AIAA journal*, Vol. 45, No. 6, 2007, pp. 1244–1257.

[17] Amsallem, D., and Farhat, C., "Interpolation method for adapting reduced-order models and application to aeroelasticity," *AIAA journal*, Vol. 46, No. 7, 2008, pp. 1803–1813.

[18] Carlberg, K., Bou-Mosleh, C., and Farhat, C., "Efficient non-linear model reduction via a least-squares Petrov–Galerkin projection and compressive tensor approximations," *International Journal for numerical methods in engineering*, Vol. 86, No. 2, 2011, pp. 155–181.

[19] Brunton, S. L., Proctor, J. L., and Kutz, J. N., "Discovering governing equations from data by sparse identification of nonlinear dynamical systems," *Proceedings of the national academy of sciences*, Vol. 113, No. 15, 2016, pp. 3932–3937.

[20] Champion, K., Lusch, B., Kutz, J. N., and Brunton, S. L., "Data-driven discovery of coordinates and governing equations," *Proceedings of the National Academy of Sciences*, Vol. 116, No. 45, 2019, pp. 22445–22451.

[21] Swischuk, R., Mainini, L., Peherstorfer, B., and Willcox, K., "Projection-based model reduction: Formulations for physics-based machine learning," *Computers & Fluids*, Vol. 179, 2019, pp. 704–717.

[22] Pearce, T., Tsuchida, R., Zaki, M., Brintrup, A., and Neely, A., "Expressive priors in Bayesian neural networks: Kernel combinations and periodic functions," *Uncertainty in artificial intelligence*, PMLR, 2020, pp. 134–144.

[23] Saad, F., Patton, B., Hoffman, M. D., Saurous, R. A., and Mansinghka, V., "Sequential Monte Carlo learning for time series structure discovery," *International Conference on Machine Learning*, PMLR, 2023, pp. 29473–29489.

[24] Vasudevan, S., Wang, X., and De Breuker, R., "Mechanism of transonic aeroelastic instabilities via synchronisation of coupled oscillators," *International Forum on Aeroelasticity and Structural Dynamics*, 2024, pp. IFASD–2024.

[25] Vasudevan, S., De Breuker, R., and Wang, X., "Manifold Learning of Nonlinear Airfoil Aerodynamics with Dimensionality Reduction," *AIAA SCITECH 2023 Forum*, 2023, p. 1199.

[26] Kalman, R. E., "A new approach to linear filtering and prediction problems," 1960.

[27] Wan, E. A., and Van Der Merwe, R., "The unscented Kalman filter," *Kalman filtering and neural networks*, 2001, pp. 221–280.

[28] Labbe, R., "GitHub - rlabbe/filterpy: Python Kalman filtering and optimal estimation library." `https://github.com/rlabbe/filterpy`, 2015. [Accessed 20-11-2024].

[29] Nixon, D., "Unsteady transonic aerodynamics," 1989.